APPLICATION OF DISCRETE FOURIER ANALYSIS OF PULSAR DATA

ELLIOTT ASHBY
PHYSICS AND ASTRONOMY
UNIVERSITY OF SOUTHAMPTON

Abstract. This paper explores the identification of pulsar signals through Fourier analysis by applying the Discrete Fourier Transform (DFT) to time-domain intensity data. By mapping temporal signal variations into frequency space, dominant periodic components of pulsar rotation can be extracted. We implement the DFT using the Goertzel algorithm and apply phase binning and de-trending techniques to increase interpretability. The analysis reveals a fundamental frequency of 59.570 ± 0.488 Hz, corresponding to a pulsar period of 0.01679 ± 0.00014s. Harmonics at 1/2f, 3/2f, and 2f support the interpretation of a rotating neutron star with a misaligned magnetic axis. These results demonstrate the utility of DFT-based frequency analysis in identifying and characterizing pulsar signals from observational data.

Contents

1. Introduction 2
2. Method 2
2.1. Theoretical Foundation 2
2.2. Implementation Details 2
3. Results 2
4. Discussion 3
4.1. Techniques 3
4.2. Comments on Results 5
5. Conclusion 6
References 9

Date: May 2025.

1. Introduction

Pulsars are a type of rapidly rotating neutron star that emit beams of electromagnetic radiation from their magnetic poles. As these beams sweep past earth during their rotation, readings will fluctuate with regularity. These periodic signals offer data about the stars themselves, tests for general relativity [1] and even capabilities as time keeping instruments [2].

This paper aims to provide analysis of an example pulsar signal to demonstrate the use of Discrete Fourier Transform (DFT) with the goal of identifying the dominant frequency components which would indicate the existence of a pulsar signal as well as determining their accuracy.

2. Method

2.1. Theoretical Foundation.

The Fourier Transform, first suggested by Jean-Baptiste-Joseph Fourier in 1822 [3], suggests that any function, discrete or continuous, can be decomposed into a series of sines and is defined like:

$$\hat{f}(\xi) = \int_{-\infty}^{\infty} f(x) e^{-i2\pi\xi x} dx \tag{2.1}$$

If we evaluate $\hat{f}(\xi)$ at all frequencies ξ we produce the frequency spectrum of the original function. However, performing an integral over a continuous domain x is only analytically possible, not computationally. We can then redefine our Fourier transform into the DFT:

$$X_k = \frac{1}{N} \sum_{n=0}^{N-1} x_n e^{-i2\pi \frac{k}{N} n} \tag{2.2}$$

If we wish, we can rewrite 2.2 as a summation of sines and cosines, and since its a linear combination we can define 2 amplitude series'.

$$\begin{aligned} A_k &= \frac{1}{N} \sum_{n=0}^{N-1} x_n \cos\left(\frac{2\pi k n}{N}\right) \\ B_k &= -\frac{i}{N} \sum_{n=0}^{N-1} x_n \sin\left(\frac{2\pi k n}{N}\right) \end{aligned} \tag{2.3}$$

2.2. Implementation Details.

In order to implement the DFT, we will use the Goertzel Algorithm [4] which, while significantly slower than any Fast Fourier Transform algorithm [5], is very simple:

Geortzel Algorithm

$$U_{N+1} = U_{N+2} = 0,$$

$$U_N = x_n + 2\cos\left(\frac{2\pi k}{N}\right) U_{n+1} - U_{n+2}, \quad \text{for } n = N, N-1 \ldots 1,$$

$$A_k = \frac{1}{N}\left[U_1 - U_2 \cos\left(\frac{2\pi k}{N}\right)\right],$$

$$B_k = \frac{-i}{N}\left[U_2 \cos\left(\frac{2\pi k}{N}\right)\right]$$

Repeat for all k in $0, 1, 2 \ldots N-1$

To test the algorithm, we generate a synthetic signal with a known cosine and sine component and plot the results as seen in 2.1.

3. Results

Performing the DFT on the dataset yields the spectrum shown in 3.1. Peak k_2 has the highest signal to noise ratio (SNR), shown in Table 1, and is the fundamental frequency $f = 59.570 \pm 0.488$. Harmonics are seen at $k_1 = 30.273 \pm 0.488$, $k_3 = 89.844 \pm 0.488$,

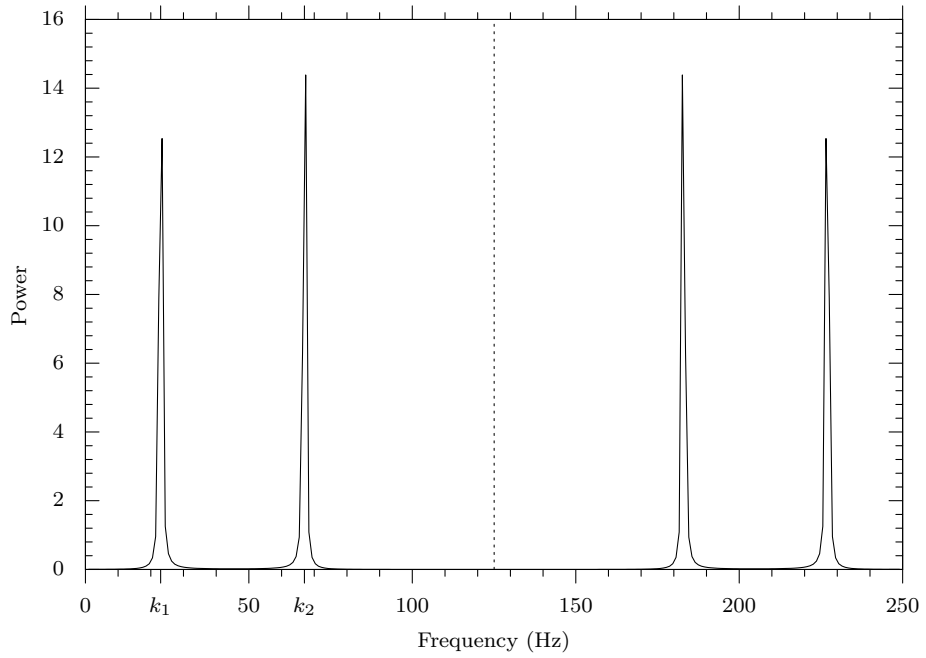

FIGURE 2.1. Fourier Transform showing the frequency series vs power of a synthetic signal of the form $f(t) = A\cos(2\pi k_1 t/N) + B\sin(2\pi k_2 t/N)$ where $k_1 = 23$ and $k_2 = 67$. The dashed line is the Nyquist frequency and the DC frequency (0Hz) has been removed.

$k_5 = 121.094 \pm 0.488$ which correspond to $1/2f$, $3/2f$ and $2f$ respectively. Additionally, the other most prominent peak is at $k_4 = 99.609 \pm 0.488$ which would be a harmonic of $5/3f$.

With a fundamental frequency of 59.570 ± 0.488 the time period of the rotation pulsar is 0.01679 ± 0.00014s. Phase binning at this frequency produces the phase-binned intensity curve shown in Figure 3.2.

Peak	Frequency [Hz]	Expected Harmonic [Hz]	Deviation [Hz]	SNR
k_1	30.273 ± 0.488	$1/2f(29.785 \pm 0.244)$	+0.488	14.8 ± 4.0
k_2	59.570 ± 0.488	f	N/A	50.9 ± 7.2
k_3	89.844 ± 0.488	$3/2f(89.355 \pm 0.732)$	+0.489	13.1 ± 3.8
k_4	99.609 ± 0.488	$5/3f(99.283 \pm 0.813)$	+0.326	9.6 ± 3.3
k_5	121.094 ± 0.488	$2f(119.14 \pm 0.976)$	+1.954	7.9 ± 3.0

TABLE 1. k_n from Figure 3.1 of the five highest SNR peaks. SNR is the signal to noise ratio.

4. Discussion

The aim of this paper was to demonstrate the use of the DFT to analyse a pulsar signal and to determine both whether the signal is a pulsar of regular rotation and also what its frequency and time period are.

4.1. Techniques. The techniques used for the analysis of the signal are, Discrete Fourier Transform (DFT) implemented in the Goertzel Algorithm, phase binning de-trending, and

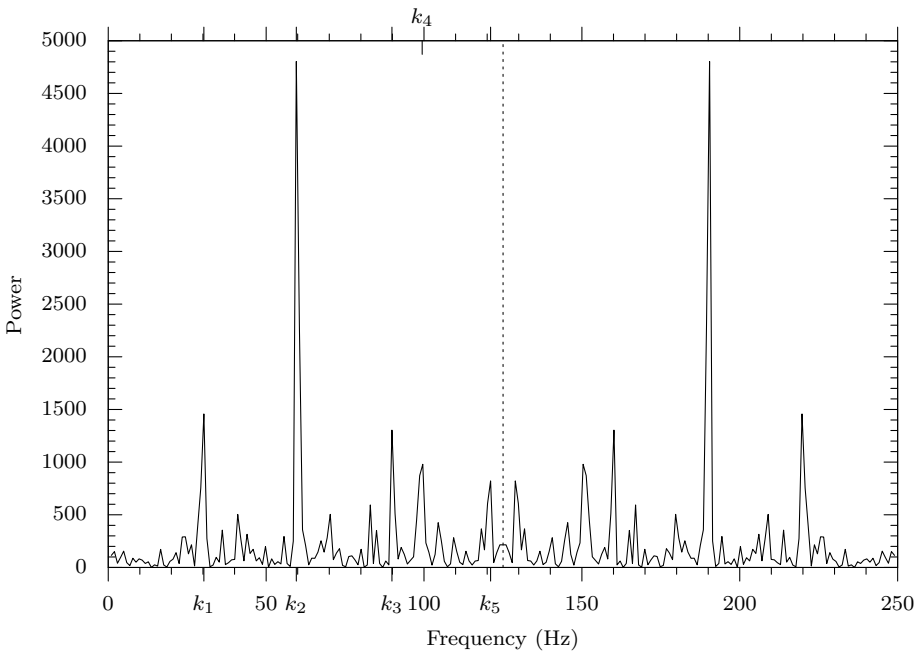

FIGURE 3.1. Fourier Transform of the dataset showing the frequency series vs power. The dashed line is the Nyquist frequency and the DC frequency (0Hz) has been removed.

synthetic data validation.

DFT allows us to determine the frequency components of the signal and their amplitude, converting the time domain signal into a frequency domain signal. In this case it was implemented using the Geortzel Algorithm which is a relatively simple implementation of the DFT that is easily programmable. Additionally the Geortzel Algorithm has a computational complexity of $O(KNM)$ vs that of the fast fourier transform (FFT) of $O(KN\log(N))$ where K is the "cost of operation" or how expensive a single step is, M is the number of DFT terms (eg. The number of frequencies) and N is naturally the number of values in the data set. Generally then it is the case that the Geortzel Algorithm is faster if:

$$M \geq \frac{5N_2}{6N}\log_2(N_2) \tag{4.1}$$

where N_2 is the N rounded up to the nearest power of 2 (since the Radix-2 FFT algorithm is most efficient when N is a power of 2). For our data with 256 entries, discounting the cost of operation for both methods, the Geortzel Algorithm is only faster if $M \leq 2$. So in our case, assuming both implementations are equally costly and if we want to calculate the DFT for all 256 DFT terms, FFT is faster. Despite this, since there are only 256 entries the scaling benefits of FFT are not significant enough to warrant its use, especially since the algorithm is only run once and not in an ongoing manner.

Phase binning is a technique used to align signal values based on phase rather than time, which is especially useful when analysing periodic signals. The signal is folded modulo the suspected period, and then averaged into bins based on phase. This emphasizes the periodic structure of the signal while reducing noise. The resulting binned profile is more interpretable, particularly when combined with de-trending.

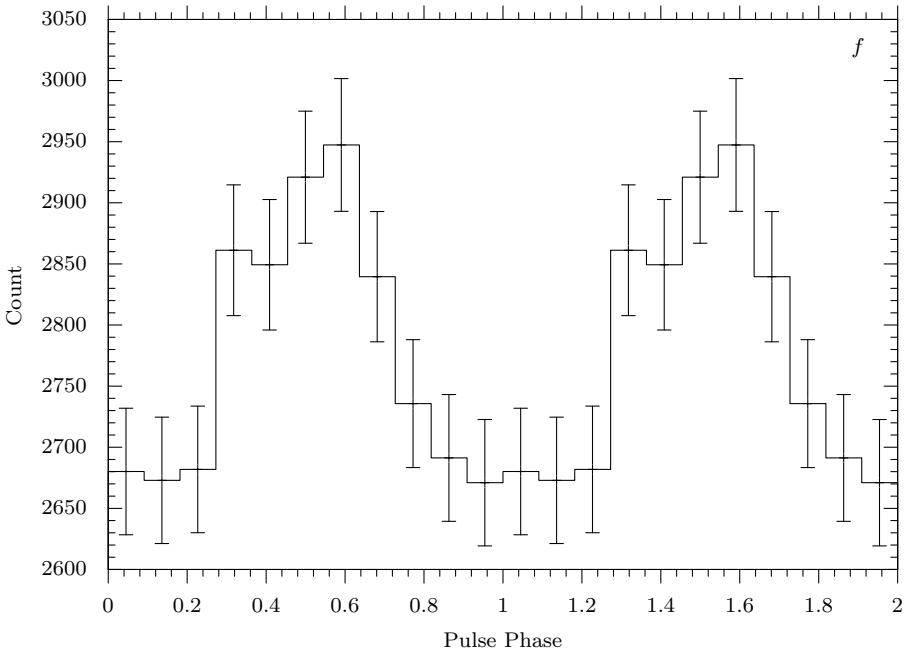

FIGURE 3.2. Phase binned intensity curve of the Fourier Transform at 59.570 Hz with 11 bins. Count is in the same arbitrary scale as the dataset and represents the intensity of the detected signal. Two phase cycles are shown for clarity and 1σ error bars are shown. The de-trended sum over all bins in a single phase is -2.094.

De-trending is a method for removing common trends from the data set leaving only the variation in the signal itself. This is done by subtracting a least-squares-fit polynomial from the data. In our analysis, we use a 0th-degree polynomial (i.e., the mean), effectively centering the data around zero and emphasizing variations relative to the average. Higher-degree polynomials could be used for more complex trends, but were unnecessary for our purposes.

Synthetic data validation involves generating artificial datasets with known properties (e.g., sinusoidal signals) and analysing them using the same functions as the real data. This allows us to verify the accuracy and correctness of our techniques. By comparing the recovered frequencies to those originally specified we can determine if the programs output is correct and or useful.

4.2. COMMENTS ON RESULTS. The results for the Discrete Fourier Transform of the dataset do suggest that the signal is a pulsar of regular rotation. And after discounting all frequencies above the Nyquist Frequency (since the frequency space is mirrored about this point and can be considered non-real negative frequencies) and removing the DC (0Hz) frequency, the most prominent frequency, and therefore the frequency most likely to be the fundamental frequency is 59.570 ± 0.488Hz with a time period of 0.01679 ± 0.00014s. The other candidate for the fundamental frequency is the peak at 30.273 ± 0.488Hz, but phase binning at this frequency reveals 2 peaks per pulse in Figure 4.1. These values are consistent with the measured pulsar being just slower than a millisecond pulsar (pulsars with a time period of less than 10ms).

For the most part, the other peaks are harmonics of $1/2f$, $3/2f$ and $2f$. A physical interpretation for the $1/2f$ and $3/2f$ harmonic could be that, due to the beams of electromagnetic radiation that are spewed from both of its magnetic poles that creates a

lighthouse effect (see Figure 4.2), the rotation axis of the pulsar could not align with its magnetic poles and we could then observe the beam at full intensity only once every two phase cycles. In this case we would observe a less intense beam every other rotation creating the $1/2f$ harmonic we see. This can be seen in Figure 4.1, there are 2 clear peaks per phase, one intense and one less intense. This backs up this interpretation that the pulsar is "wobbling" or processes as it rotates relative to earth.

The $5/3f$ harmonic however is the only harmonic that is not a multiple of the fundamental frequency. One possible interpretation is that, due to its closeness to 100Hz, it could be noise from monitoring equipment or perhaps it could be the fundamental frequency of another pulsar and the main pulsar we observe could be part of a binary system.

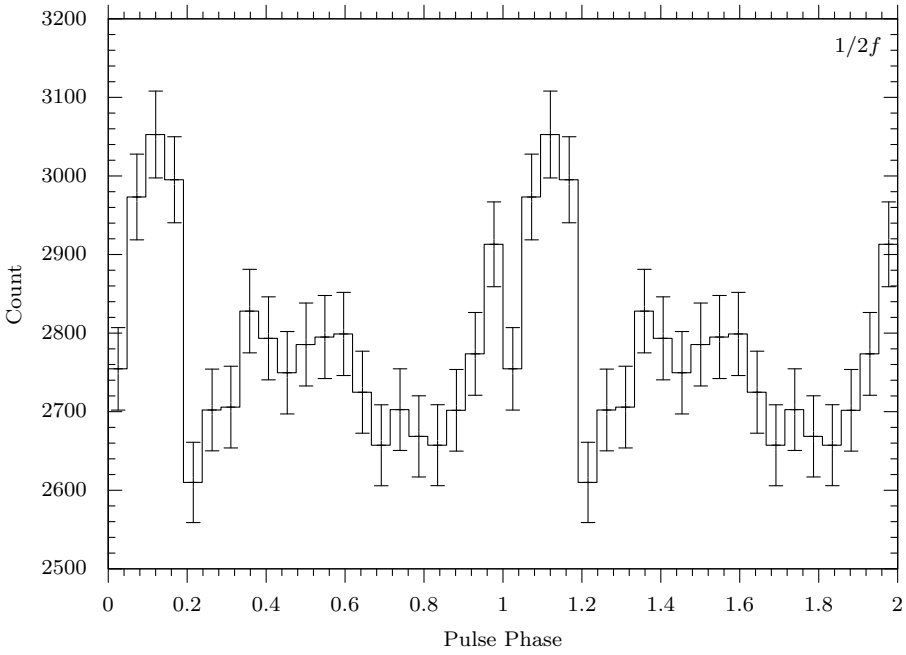

FIGURE 4.1. Phase binned intensity curve of the Fourier Transform at 30.273 Hz with 21 bins. Count is in the same arbitrary scale as the dataset and represents the intensity of the detected signal. Two phase cycles are shown for clarity and 1σ error bars are shown.

5. Conclusion

In this paper, we demonstrated the use of the Discrete Fourier Transform (DFT) for the analysis of pulsar signals using the Geortzel Algorithm. By applying this to the intensity time data in the dataset we successfully identified the fundamental frequency and its harmonics, confirming the presence of a regularly rotating pulsar. The fundamental frequency is detected at 59.570 ± 0.488 Hz, with a period of 0.01679 ± 0.00014s and aligns with the expected properties of a slightly slower rotating millisecond pulsar. This analysis also revealed the presence of harmonic components, including $1/2f$, $3/2f$ and $2f$. The presence of the $1/2f$ and $3/2f$ harmonics support the interpretation of non-aligned processing pulsar, however the presence of the $5/3f$ harmonic may not be a harmonic at all and instead could be noise or the influence of a secondary signal source.

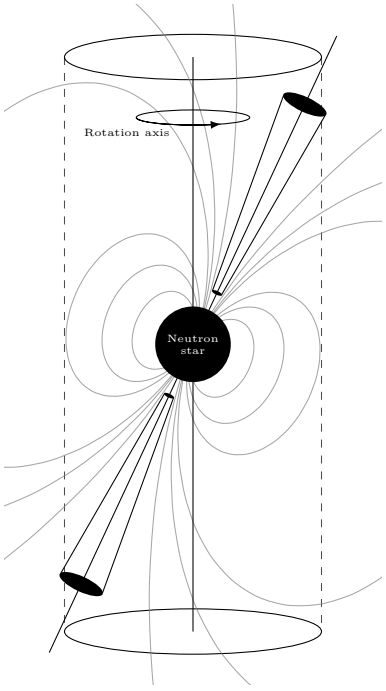

FIGURE 4.2. A diagram of a pulsar with magnetic poles misaligned with the rotation axis. Rotation will create a "lighthouse" effect as the EM emission beams sweep past the earth. Sourced from [6].

This paper highlights the effectiveness of the DFT as a tool for analysing pulsars, despite the computation limitations of the Geortzel Algorithm. Additionally, the use of phase binning and de-trending techniques can further enhance the interpretability of the results, providing more accurate analysis of pulsar signals.

Future work could include the implementation of the FFT algorithm, which is more efficient for large datasets and would allow for the analysis of pulsar signals with a time period of less than a millisecond with greater accuracy. Additionally, the dataset used only includes data at a single, unknown, energy band; taking readings at different energy bands and using that to inform analysis could reveal additional relationships as well as clarifying observations like the $5/3f$ peak.

APPENDIX A. ADDITIONAL USES OF INTEGRATION, RUNGE-KATTA AND FOURIER TRANSFORMS

N-BODY SIMULATIONS. In computational astrophysics, Hernandez and Bertschinger [7] note that calculating long-term evolutions (eg. galaxy formation and planetary orbits) have no known analytical solutions so researchers use various numerical solutions. Hernandez and Berschinger propose a method of time-symmetric integration to predict complex dynamical behaviour in astrophysics.

THE MAGNETOCALORIC EFFECT. In this paper Moore, Skokov, Liu and Gutfleisch [8] present a method of numerically integrating measured entropy or temperature data to evaluate the magnetocaloric effect in a magnetic cooling cycle.

A GENERAL QUANTUM ALGORITHM FOR NUMERICAL INTEGRATION. In this paper Shu, Shan, Xu, Zhao and Wang [9] present a general quantum algorithm for numerical integration. Typical

methods of classical integration algorithms are at most computational complexity of $O(N)$ but by quantum encoding of integrable functions through polynomial approximation and constructing a quantum oracle to discretise and mark locations the integration area the computational complexity can be reduced to $O(\sqrt{N})$.

Effective Force on the mast of Racing Sail-boats. Since wind forces vary as a function of distance from the deck on sails, it is required to calculate the tensile strength needed for the cables holding the mast. Since the functions required to be integrated are difficult to analytically solve, numerical methods like the trapezoidal rule and Simpsons 1/3 rule must be used. [10]

Coulomb Counting. The available capacity of a battery can be determined by integration of the current drawn from the battery over time. However, since other factors like temperature and current direction can influence the capacity of batteries, numerical integration methods are required. [11]

Industrial Instrumentation. In industrial instrumentation, the calculation of the accumulation of some fluid from a measured flow rate is a common task. Often times this can implemented mechanically through an odometer-style device which uses rotational elements and a ratchet mechanism to mechanically integrate the movement of the rotational input. [12]

Runge-Kutta Methods for Robot Arm & Initial Value Problem. Senthilkumar et al. [13] present a Runge-Kutta(5,5) method for solving the robot arm and initial value problem. Robot arms equations of motions are often complex ODEs due to the many different variables involved in physical processes so accurate numerical methods like using Runge-Kutta reduce the error in predicting the arm's position, velocity and acceleration over time.

Streamline and Streamtube Visualization. In fluid dynamics simulations, the visualization of flow characteristics such as streamlines and streamtubes is crucial for understanding complex fluid behaviors. The construction of these visual elements often requires efficient numerical methods for tracing particle paths over time. Ueng et al. [14] introduce a specialized Runge-Kutta integration method to enhance the speed and accuracy of particle path tracing, making it significantly faster than traditional methods like Runge-Kutta (2,4) and (4,4). Their approach, designed for unstructured grids, is especially beneficial when working with large-scale fluid simulations that require the visualization of intricate flow patterns.

Numerical Solution of Nonlinear Schrodinger Approaches Using the Fourth-Order Runge-Kutta Method for Predicting Stock Pricing. In this paper, Kartono et al. [15] present a numerical solution of non-linear Schrödinger approaches to stock pricing using the Fourth-Order Runge-Kutta. The method is based on the idea of using the Runge-Kutta method to approximate the solution of the non-linear Schrödinger equation, which is a widely used method in finance for modelling stock prices.

The Application of Runge Kutta Fourth Order Method in SIR Model for simulation of COVID-19 Cases. In this paper, Iskandar and Tiong [16] use Runge-Kutta numerical methods to approximate covid cases over time. This approach ensures accurate integration of the ODEs, accounting for time-dependent variables like infection rates and quarantine efficacy. Real-world changes are accounted for and provides reliable forecasts for outbreak progression.

Operational Orbit Determination. Space mission engineers propagate orbits using Runge–Kutta integrators. For example, Artemis lunar orbit determination employs a high-order Runge–Kutta (7/8) integrator to propagate the spacecraft state between manoeuvres. [17]

Autonomous Vehicle Technologies for Small Fixed-Wing UAVs. In small-UAV guidance systems, it's common to use RK4 integration for state propagation. In these designs, the UAV's kinematic equations are integrated in real-time using a 4th-order Runge–Kutta method. This approach allows the autopilot to generate feasible, time-efficient flight paths directly onboard the aircraft. [18]

Medical Image Reconstruction with the FFT. This chapter in GPU Gems 2 [19] introduces the use of the FFT to reconstruct medical images. The FFT is particularly useful for medical imaging where the data is often complex and contains many redundant information. Utilising the GPU and CUDA allows the FFT to be processed in parallel allowing for a massive speed up.

Fourier Transform Spectroscopy. In this paper, Paschotta [20] lays out The technique involves sending electromagnetic radiation, typically infrared light, into a Michelson interferometer and measuring the output power as the mirror moves, changing the arm length. For monochromatic light, the power oscillates sinusoidally with arm length, while polychromatic light produces a complex interferogram. Applying a Fourier transform to this data reveals the optical spectrum, showing the power distribution across wavelengths, though spectral phase information is not obtained.

Full-field Brillouin microscopy based on an imaging Fourier-transform spectrometer. In this paper, Bevilacqua and Prevedel [21] present a new imaging Fourier-transform spectrometer for enhanced Brilllouin microscopy allowing for three-dimensional, all-optical and non-contact techniques to assess the mechanical properties of biological samples.

On discrete cosine transform. In this paper, Zhou [22] describes the discrete cosine transform (DCT) developed originally by Nasir Ahmed, which is a lossy compression algorithm that relies on the discrete Fourier transform to pick out data of high importance allowing the algorithm to preserve data fidelity while minimizing file size. This is used widely in medical imaging systems like MRI and CT scans where data output is very large but all scans should be kept.

Bearing vibration detection and analysis using enhanced fast Fourier transform algorithm. In this paper, Lin et al. [23] look at bearing defects that create irregular, cyclostationary vibration pulses, often caused by roller slippage, and determine whether smarter Fast Fourier Transforms can be used to predict breakages for predictive maintenance. It works by modelling how major frequencies and spectral leakage interact, helping pinpoint faults accurately.

Real Time Pitch Detection For Vocal Tuning Using FFT Algorithm And Spectrogram. In this paper, Noak and Darmawan [24] present a real-time pitch detection algorithm using the Fast Fourier Transform (FFT) and spectrogram. The FFT is used to analyse the frequency content of the audio signal, while the spectrogram is used to visualize the frequency content over time. This allows for real-time pitch detection and tuning, which is crucial for applications like music production and audio processing.

References

[1] Weisberg, J. M. ; Taylor, J. H. ; Fowler, L. A.: Gravitational waves from an orbiting pulsar. In: *Scientific American* 245 (1981), Oktober, S. 74–82. http://dx.doi.org/10.1038/scientificamerican1081-74. – DOI 10.1038/scientificamerican1081–74

[2] BACKER, D. C.: The 1.5-Millisecond Pulsar. In: *Annals of the New York Academy of Sciences* 422 (1984), Nr. 1, 180-181. http://dx.doi.org/https://doi.org/10.1111/j.1749-6632.1984.tb23351.x. – DOI https://doi.org/10.1111/j.1749–6632.1984.tb23351.x

[3] Fourier, J.B.J.: *Théorie analytique de la chaleur*. Didot, 1822 (Landmarks of Science). https://books.google.co.uk/books?id=TDQJAAAAIAAJ

[4] Goertzel, Gerald: An Algorithm for the Evaluation of Finite Trigonometric Series. In: *The American Mathematical Monthly* 65 (1958), Nr. 1, 34–35. http://www.jstor.org/stable/2310304. – ISSN 00029890, 19300972

[5] Cooley, James W. ; Tukey, John W.: An Algorithm for the Machine Calculation of Complex Fourier Series. In: *Mathematics of Computation* 19 (1965), Nr. 90, 297–301. http://www.jstor.org/stable/2003354. – ISSN 00255718, 10886842

[6] Knierim, Anno: *aknierim/TikZ_assortment: Assortment of TikZ graphics/source code.* http://dx.doi.org/10.5281/zenodo.11045574. Version: April 2024

[7] Hernandez, David M. ; Bertschinger, Edmund: Time-symmetric integration in astrophysics. In: *Monthly Notices of the Royal Astronomical Society* 475 (2018), Januar, Nr. 4, 5570–5584. http://dx.doi.org/10.1093/mnras/sty184. – DOI 10.1093/mnras/sty184. – ISSN 1365–2966

[8] Moore, J. D. ; Skokov, K. P. ; Liu, J. ; Gutfleisch, O.: Procedure for numerical integration of the magnetocaloric effect. In: *Journal of Applied Physics* 112 (2012), 09, Nr. 6, 063920. http://dx.doi.org/10.1063/1.4754561. – DOI 10.1063/1.4754561. – ISSN 0021–8979

[9] Shu, Guoqiang ; Shan, Zheng ; Xu, Jinchen ; Zhao, Jie ; Wang, Shuya: A general quantum algorithm for numerical integration. In: *Scientific Reports* 14 (2024), 10432. http://dx.doi.org/10.1038/s41598-024-61010-9. – DOI 10.1038/s41598–024–61010–9

[10] Chapra, Steven C. ; Canale, Raymond P.: Case Studies: Numerical Integration and Differentiation. In: *Numerical Methods for Engineers*. 6th. McGraw-Hill, 2010, Kapitel 24, S. 675–677. – Accessed from https://lms.su.edu.pk/download?filename=1588353167-case-studies-nd-and-ni-numerical-methods-for-engineers-chapra-canale.pdf&lesson=7570

[11] Stefanopoulou, A.G. ; Kim, Y.: 10 - System-level management of rechargeable lithium-ion batteries. Version: 2015. http://dx.doi.org/https://doi.org/10.1016/B978-1-78242-090-3.00010-9. In: Franco, Alejandro A. (Hrsg.): *Rechargeable Lithium Batteries*. Woodhead Publishing, 2015 (Woodhead Publishing Series in Energy). – DOI https://doi.org/10.1016/B978–1–78242–090–3.00010–9. – ISBN 978–1–78242–090–3, 281-302

[12] Control.com Editorial Team: *Numerical Integration*. https://control.com/textbook/calculus/numerical-integration. Version: 2025. – Accessed: 2025-05-08

[13] Senthilkumar, Sukumar ; Lee, Malrey ; Kwon, Tae-Kyu: Runge-Kutta(5,5) Methods for Robot Arm & Initial Value Problem. In: *International Journal of Control and Automation* 6 (2013), Nr. 3. https://article.nadiapub.com/IJCA/vol6_no3/30.pdf

[14] Ueng, S. K. ; Sikorski, K. ; Ma, Kwan-Liu: Fast Algorithms for Visualizing Fluid Motion in Steady Flow on Unstructured Grids / NASA. Version: 1995. https://ntrs.nasa.gov/api/citations/19960002576/downloads/19960002576.pdf. NASA Ames Research Center, 1995 (NASA-CR-198198). – Forschungsbericht. – ICASE-95-58

[15] Kartono, A ; Fatmawati, V W. ; Wahyudi, S T. ; Irmansyah: Numerical Solution of Nonlinear Schrodinger Approaches Using the Fourth-Order Runge-Kutta Method for Predicting Stock Pricing. In: *Journal of Physics: Conference Series* 1491 (2020), mar, Nr. 1, 012021. http://dx.doi.org/10.1088/1742-6596/1491/1/012021. – DOI 10.1088/1742–6596/1491/1/012021

[16] Iskandar, Danial ; Tiong, Ong C.: The Application of Runge Kutta Fourth Order Method in SIR Model for simulation of COVID-19 Cases, Proc. Sci. Math., 2022, 61–70

[17] Woodard, Mark ; Cosgrove, Daniel ; Morinelli, Patrick ; Marchese, Jeffrey ; Owens, Brandon ; Folta, David: Orbit Determination of Spacecraft in Earth-Moon L1 and L2 Libration Point Orbits. In: *Advances in the Astronautical Sciences* 142 (2011), 01, S. 1683

[18] Beard, Randal ; Kingston, Derek ; Quigley, Morgan ; Snyder, Deryl ; Christiansen, Reed ; Johnson, Walt ; McLain, Tim ; Goodrich, Michael: Autonomous Vehicle Technologies for Small Fixed-Wing UAVs. In: *Journal of Aerospace Computing, Information, and Communication* 2 (2005), 02. http://dx.doi.org/10.2514/1.8371. – DOI 10.2514/1.8371

[19] Sumanaweera, Thilaka ; Liu, Donald: Medical Image Reconstruction with the FFT. Version: 2005. https://developer.nvidia.com/gpugems/gpugems2/part-vi-simulation-and-numerical-algorithms/chapter-48-medical-image-reconstruction. In: *GPU Gems 2*. 2005, Chapter 48

[20] Paschotta, R.: *Fourier Transform Spectroscopy*. RP Photonics Encyclopedia. http://dx.doi.org/10.61835/seo. Version: 2019

[21] Bevilacqua, C. ; Prevedel, R.: Full-field Brillouin microscopy based on an imaging Fourier-transform spectrometer. In: *Nature Photonics* 19 (2025), S. 494–501. http://dx.doi.org/10.1038/s41566-025-01619-y. – DOI 10.1038/s41566–025–01619–y

[22] Zhou, Jianqin: *On discrete cosine transform*. https://arxiv.org/abs/1109.0337. Version: 2011

[23] Lin, Hsiung ; Ye, Yu-Chen ; Huang, Bo-Jyun ; Su, Jia-Lun: Bearing vibration detection and analysis using enhanced fast Fourier transform algorithm. In: *Advances in Mechanical Engineering* 8 (2016), 10. http://dx.doi.org/10.1177/1687814016675080. – DOI 10.1177/1687814016675080

[24] Noak, Devin ; Darmawan, I Dewa Made Bayu A.: Real Time Pitch Detection For Vocal Tuning Using FFT Algoritma And Spectrogram. In: *JELIKU (Jurnal Elektronik Ilmu Komputer Udayana)* 8 (2020), 01, S. 325. http://dx.doi.org/10.24843/JLK.2020.v08.i03.p15. – DOI 10.24843/JLK.2020.v08.i03.p15